

Understanding Coating Thickness and Uniformity of Blade-Coated SnO_2 Electron Transport Layer for Scalable Perovskite Solar Cells

Severin Siegrist, Pranjal Nandi, Radha K. Kothandaraman, Aribia Abdessalem, Ayodhya N. Tiwari, and Fan Fu*

The low-cost and fully solution-based perovskite photovoltaic devices can be upscaled by using the blade coating method. However, control of the charge transport layers thickness on nanometer scale is challenging since the inherent nature of the blade coating process unavoidably induces thickness gradients along the coating direction of blade coated layer. Herein, the film thickness and the uniformity of blade-coated SnO_2 colloidal dispersions in the Landau–Levich regime are systematically studied by varying the substrate temperature, the dispensed solution volume, and the solution concentration as well as the coating speed. It is shown that the advancing meniscus height heavily influences the SnO_2 film thickness. As the solution is consumed during the coating process, the meniscus height decreases and hence the film thickness, yielding poor uniformity of the blade-coated layer. To improve the thickness uniformity, the dispensed solution volume is used to reduce the alteration of the advancing meniscus height along the coating direction and minimize the capillary flow with the appropriate substrate temperature. This study provides crucial insights toward the successful upscaling of perovskite solar cells by blade coating.

1. Introduction

The high-efficiency metal halide perovskite solar cells (PSCs) have been developed with different deposition methods and certified power conversion efficiencies (PCE) up to 25.7% have been demonstrated on 0.1 cm^2 area.^[1–5] However, the device performance sharply drops, when the active area is increased from lab-scale pixels ($<0.1 \text{ cm}^2$, 25.7%) to fab-scale modules ($>800 \text{ cm}^2$, 17.9%), which is attributed to the inhomogeneity


in functional layers on large-area substrates,^[6] especially when coated with methods, such as spin coating, with inherent limitations for scale up. The solution-based methods for manufacturing of PSCs are attractive because of low capex, high throughput production, and excellent material usage. The most common, scalable, and solution-based method is blade coating due to its fast solution screening capability and ease of use.^[7] This method has been applied for coating different perovskite compositions and various charge transport material layer.^[8–11] However, most works have focused on studying perovskite crystallization and film formation process, but paying less attention to the charge transport layers.

Among various charge transport materials, SnO_2 as an n-type semiconducting oxide material has attracted attention due to its wide bandgap (3.6–4.0 eV) with high transmittance, high electron mobility (up to $240 \text{ cm}^2 \text{ V}^{-1} \text{ s}^{-1}$), chemical stability, low-temperature processability ($<200^\circ\text{C}$), its proper band alignment with common perovskites, and low cost.^[12] SnO_2 has been used in many record-efficiency single-junction PSCs.^[1,13,14] However, the SnO_2 in such devices is generally deposited either by spin coating, which is not regarded as scalable deposition method due to its nonuniformity from center to edge as well as its poor solution usage, or by chemical bath deposition (CBD), which is a time-consuming deposition method, generating a lot of solution waste and potentially stalling a high throughput production of PSCs.^[1,14,15] A more cost-effective and industry-relevant approach is the use of commercially available SnO_2 colloidal solution deposited by meniscus-guided methods, such as blade coating or slot-die coating.^[16–18] Using these methods to achieve high-efficiency solar modules requires a thorough understanding of the deposition process to control the uniformity and thickness of the layer in the range of nanometers all across the large area substrate.^[19]

In this work, we blade coat SnO_2 colloidal solution to perform in-depth investigation of the individual blade coating parameters and how they affect the dried film thickness and uniformity in the nanometer range. We find that the substrate temperature has a strong influence on film thickness—blade coating at low temperatures (relative to the boiling point of the solvent) can locally increase

S. Siegrist, P. Nandi, R. K. Kothandaraman, A. Abdessalem, A. N. Tiwari, F. Fu

Laboratory for Thin Films and Photovoltaics
Empa - Swiss Federal Laboratories for Materials Science and Technology
Ueberlandstrasse 129, 8600 Dübendorf, Switzerland
E-mail: fan.fu@empa.ch

 The ORCID identification number(s) for the author(s) of this article can be found under <https://doi.org/10.1002/solr.202300273>.

© 2023 The Authors. Solar RRL published by Wiley-VCH GmbH. This is an open access article under the terms of the Creative Commons Attribution-NonCommercial License, which permits use, distribution and reproduction in any medium, provided the original work is properly cited and is not used for commercial purposes.

DOI: 10.1002/solr.202300273

the dried film thickness by about 50%, compared to higher coating temperatures, but adversely affects the film uniformity due to capillary flow. We further show the influence of the dispensed solution volume on film thickness and how it can be used to improve the uniformity by minimizing alterations of the advancing meniscus height along the coating direction. Moreover, the film uniformity is also affected by the angle of the blade. Furthermore, we show how each blade coating parameter can be used to control the film thickness. Finally, a modification of the blade coater is presented to further improve the uniformity, and we point out the necessity of a deposition process with continuous solution supply (e.g., slot-die coating) to commercialize PSCs successfully.

2. Results and Discussion

In blade coating method, the solution is dispensed on the front side of the blade where it runs down, wets the substrate, and fills the gap between the substrate and the blade by capillary flow. During this process, two menisci form, the advancing and the receding meniscus. While the advancing meniscus, which determines the dynamic wetting process, is critical for determination of optimum coating speed, the receding meniscus influences the quality of the coated film.^[20,21] In **Figure 1a**, the schematics of blade coating process are illustrated. The geometry of the advancing meniscus depends on the wetting angles θ_1 and θ_2 , its height H , and the substrate width. Substrate-related properties, which affect the contact angle θ_1 , are separately discussed in Note S3, Supporting Information. The remaining parameters are specific to the blade geometry, such as the blade angle α or to the deposition parameters, e.g., the gap G or the blading speed U .

For the blade coating process, two coating regimes exist, the evaporation and the Landau–Levich regime. For high throughput production, the latter regime is of importance as it describes the coating dynamics at high blading speeds. It is characterized by the excessive rate of solvent supply relative to the rate of solvent evaporation.^[22] The contact line, where film solidification takes place, lags far behind the receding meniscus, such that casting, leveling, and drying are temporally separated processes.^[21] In the Landau–Levich regime, the wet film thickness t_{wet} is determined by

$$t_{\text{wet}} = c_1 L \left(\frac{\mu U}{\gamma} \right)^{2/3} = c_1 L (Ca)^{2/3} \quad (1)$$

with a numerical constant c_1 , the characteristic length L , the coating speed U , the viscosity μ , the surface tension γ of the solution, and the capillary number Ca .^[20,22,23] This wet film thickness defines the total amount of solute that is dragged onto the substrate by the coating process. During the solidification process, solvents evaporate while the solutes remain on the substrate, which forms a compact film of dry film thickness t_{dry} , yielding the final film thickness. In the following sections, we highlighted that the drying process is of equal importance for the final film thickness as the coating process and we systematically study the influence substrate temperature, dispensed solution volume, coating speed, and the solution concentration on the dry film thickness t_{dry} to demonstrate how each parameter can be used to control the final film thickness of the blade-coated layer.

2.1. Impact of the Substrate Temperature

It is important to first identify the substrate temperature window, which allows quick solvent evaporation to minimize the microscopic flows in the as-deposited wet films. These capillary flows transport additional solutes to the proceeding solidification front, which can deteriorate the uniformity of the blade-coated film. Therefore, we investigated different substrate temperatures while fixing the blading speed to 30 mm s^{-1} . The knowledge about the solvent, in this case, water with a boiling point of 100°C , gives already a parameter space of the substrate temperature, ranging from 40°C to 90°C , to be screened. For each temperature, thickness is measured at specific positions along the blade coating direction: 10, 20, and 30 mm away from the starting line of the blade coating process (cf. inset in **Figure 1b**). The results are summarized in **Figure 1b**. At low substrate temperatures ($<50^\circ\text{C}$), the drying of the as-coated film takes longer and the films are roughly 20 nm thicker compared to those obtained at higher substrate temperature ($>60^\circ\text{C}$). This is attributed to lower solvent evaporation rates prolonging solidification of the film at low substrate temperatures. In slow drying processes, more solute can be transported from the meniscus to

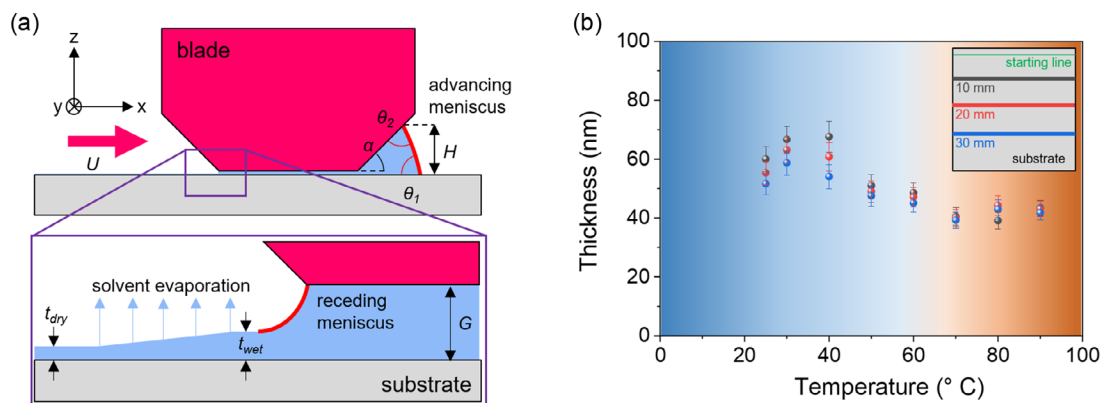


Figure 1. a) Schematics of the blade coating process with indicated geometrical parameters. b) SnO₂ film coated at different substrate temperatures. The dried film thickness is measured at three coating distances, 10 mm (black), 20 mm (red), and 30 mm (blue) from the starting point. The data points show the mean value of a triangular scan pattern, refer to Note S1, Supporting Information, for details.

the contact line by capillary flow (cf. coffee-ring effect), while at higher substrate temperatures, this transport is limited as the drying process is quicker.^[24,25] Moreover, the high concentration of solute near the contact line increases the surface tension, which transports more solute to the solidification edge by Marangoni flow.^[21] Furthermore, due to the heated substrate, a secondary Marangoni flow establishes, which transports solute in the opposite direction to the bulk solution due to thermal gradients.^[21,26,27] These flows are illustrated in Figure S1, Supporting Information. Moreover, for substrate temperatures below 50 °C, the measured thicknesses decrease along the coating direction and prolonged drying is observed. During the prolonged drying, capillary flows are active and carry solutes of the wet film to the solidification front. As the solidification front gradually moves across the substrate, the wet film area shrinks and fewer solutes are available that can be transported to the solidification front, resulting in reduced thicknesses along the coating direction. Therefore, the drying process must be quick to suppress capillary flows and achieve better uniformity of the films, by choosing substrate temperature closer to the boiling point of the solvent, in this case, 70 °C. Alternatively to hot casting, a quick solvent evaporation can also be achieved by (hot) gas-assisted drying using a gas knife.^[18]

For hot casting at 70 °C, the dispensed solution quickly heats up, therefore the time between dispensing the solution and initiation of the blade coating process may also affect the film uniformity. Thus, to elucidate the influence of the solution tempering on the drying process, we also investigate the effect of resting times (time between solution dispensing and start moving of the blade) of the solution on the substrate, at 40 and 70 °C substrate temperature. The measured thickness and the transmittance of the dried SnO₂ films are presented in Figure S2 and S3, Supporting Information. All films coated at 40 and at 70 °C with varying resting times (solution tempering) ranging from 1 to 9 s show no changes in the thickness and transmittance. Furthermore, AFM measurements (Figure S4, Supporting Information) of these films yield similar surface roughness for both substrate temperatures with solution tempering of 7 s. However, SEM top-view images reveal more favorable aggregation of SnO₂ nanocrystals, when low coating temperatures (e.g. 40 °C) are used (Figure S5a, Supporting Information), in contrast to 70 °C coating temperature (Figure S5b, Supporting Information). To conclude the influence of the substrate temperature on the film quality, 70 °C is promising due to the improved film thickness uniformity along the coating direction due to minimized capillary flows.

2.2. Impact of the Volume

After finding the substrate temperature window to minimize capillary flows in the SnO₂ wet film, we further elucidate additional parameters that affect the dried film thickness. Le Berre et al. showed that the characteristic length is described by the reciprocal of the receding meniscus' curvature.^[22,23] In Equation (1), the characteristic length L scales linearly with the wet film thickness t_{wet} . As there is no lateral pressure gradient, the curvature of the receding meniscus equates to the curvature of the advancing meniscus and the characteristic length can be expressed as

$$L = \frac{H}{\cos \theta_1 + \cos \theta_2 - \frac{H^2}{2\kappa^2}} \quad (2)$$

with the contact angles θ_1 and θ_2 , the capillary length κ , and the height of the advancing meniscus H as indicated in Figure 1a.^[22,28] To demonstrate the influence of the meniscus height on the dried film thickness, we dispense different solution volumes to blade coat SnO₂ films on UV-Ozone (UVO) treated glass with 30 mm s⁻¹ at 70 °C (black) and 40 °C (red) substrate temperatures, respectively. Figure 2a summarizes the dried thicknesses of the SnO₂ film as a function of the dispensed solution volume.

We observe that the dispensed volume can be used to alter the dry film thickness of the blade-coated layer, independently of the substrate temperature. Furthermore, the films deposited at 40 °C are thicker than the films at 70 °C for any dispensed volume. A similar trend is observed in the transmittance measurements of these films, as shown in Figure S6 and S7, Supporting Information. For both temperatures, the transmittance is decreasing for larger dispensed solution volumes, indicating increasing film thicknesses. But for 40 °C, internal reflections are observed already for dispensed volumes as small as 50 µL, which shifts toward longer wavelengths when dispensed volumes are further increased. Contrary, at 70 °C substrate temperature, the internal reflections start to occur for dispensed volumes larger than 90 µL. This temperature-dependent thickness variation is caused by capillary flows, which can be modulated by the substrate temperature.

So far, the characteristic length L was assumed to be constant during the blade coating process. However in reality, the advancing meniscus height decreases as the solution is consumed during the blade coating process. This reduction in meniscus height induces a thickness gradient along the coating direction, adversely hampering the uniformity of large-area coatings of functional layers needed for perovskite solar modules. Here, we present ways to minimize solution consumption and thus the thickness gradient, e.g., by reducing the viscous drag, using smaller angles α or dispensing larger volumes. The consumed solution volume V_c per millimeter of coating length for a substrate width W is calculated as

$$\frac{V_c}{\text{mm}} = t_{\text{wet}} \cdot W \quad (3)$$

For simplicity, we assume V_c to be constant along the coating direction. The wet film thickness t_{wet} is computed by using

$$t_{\text{wet}} = t_{\text{dry}} \cdot \frac{\frac{w_{\text{solute}} + w_{\text{solvent}}}{\rho_{\text{solute}} + \rho_{\text{solvent}}}}{\frac{w_{\text{solute}}}{\rho_{\text{solute}}}} \quad (4)$$

with weight fraction w and density ρ .^[28] Here, instantaneous drying is assumed and the time-dependent factor affecting the dried film thickness t_{dry} by the capillary flow is neglected. In Figure S8, Supporting Information, the consumed solution volume V_c is plotted against the dried film thicknesses t_{dry} for different concentrations of the solution (in wt%) w_{solute} . For example, to obtain a dried SnO₂ film of 40 nm with a 4.14 wt% concentrated solution, roughly 0.33 µL mm⁻¹ is consumed for a given coating width of 50 mm. The solution concentration can be used to

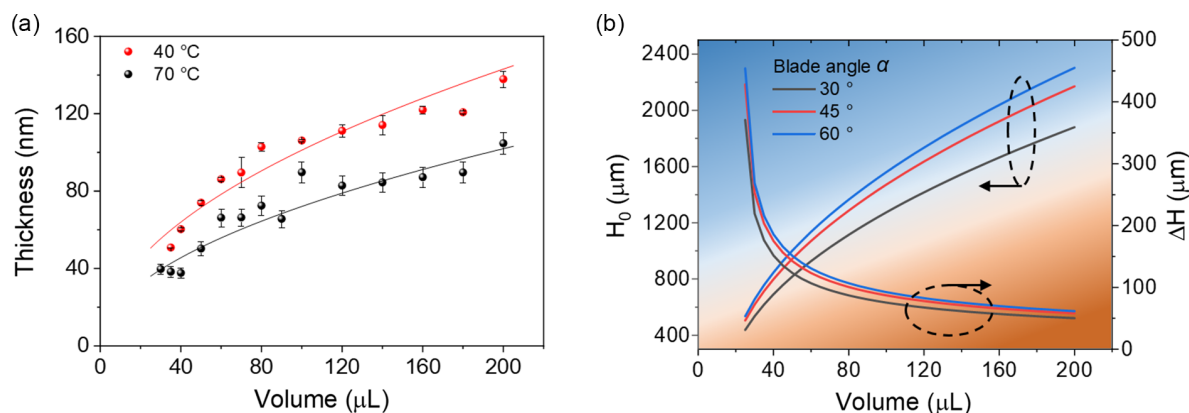


Figure 2. a) Dried film thicknesses for various dispensed solution volumes at 70 °C (black) versus 40 °C (red) substrate temperature. A triangular scan (cf. Figure S24, Supporting Information) is done in the center of the substrate. b) Overview of the advancing meniscus height at the start of the blade coating process (H_0) and of the change of the meniscus height $\Delta H = H_0 - H_{30}$ over 30 mm coating length (H_{30}) for different blade angles α and various dispensed solution volumes. Details are provided in Note S2 and Figure S25, Supporting Information.

minimize the consumed solution volume during the coating for a given dried film thickness. Apart from that, reducing the viscous drag by lowering the blading speed, using smaller angles α or dispensing larger volumes are other ways to minimize solution consumption. Plots in Figure 2b show the initial meniscus height H_0 dependence on dispensed solution volume for different blade angles α . With smaller angles, H_0 is smaller. Next, the difference of the meniscus height at the initial position and at 30 mm of coating length, i.e., $\Delta H = H_0 - H_{30}$ is computed. For detailed calculations, refer to Note S2, Supporting Information. While for smaller volumes, this difference is large and results in inhomogeneous films, larger volumes, and a smaller blade angle improve the uniformity as the difference of the meniscus height reduces dramatically.

Alternatively, the blade coater can be modified with a solution reservoir attached to the blade, as illustrated in Figure S9, Supporting Information. With a small reservoir angle β , the change of the meniscus height along the coating direction can be reduced and more uniform coatings can be obtained.

2.3. Impact of the Blade Coating Speed

We now turn the focus on the coating speed U , which has been investigated in previous works with different materials, but not yet for colloidal dispersion of SnO₂ nanoparticles.^[19,29,30] To probe this relation for colloidal dispersions, we vary the coating speed, while maintaining a fixed volume and gap at a constant substrate temperature. The dried film thickness is plotted as a function of the coating speed, as shown in Figure 3a.

Beyond 10 mm s⁻¹, the film thickness increases with higher coating speeds, showing that the coating process takes place in the Landau–Levich regime. The power function fit yields an exponent of 0.66, which is in good agreement with Equation (1). Due to higher coating speeds, viscous forces dominate over surface tension, and a liquid film is dragged out from the coating meniscus. The drying of this liquid film (observed by eye) takes longer with increasing speed, since the wet film thickness increases accordingly. This further confirms that the coating takes place in the Landau–Levich regime, as the amount of the solvent deposited on the substrate is larger than the amount of

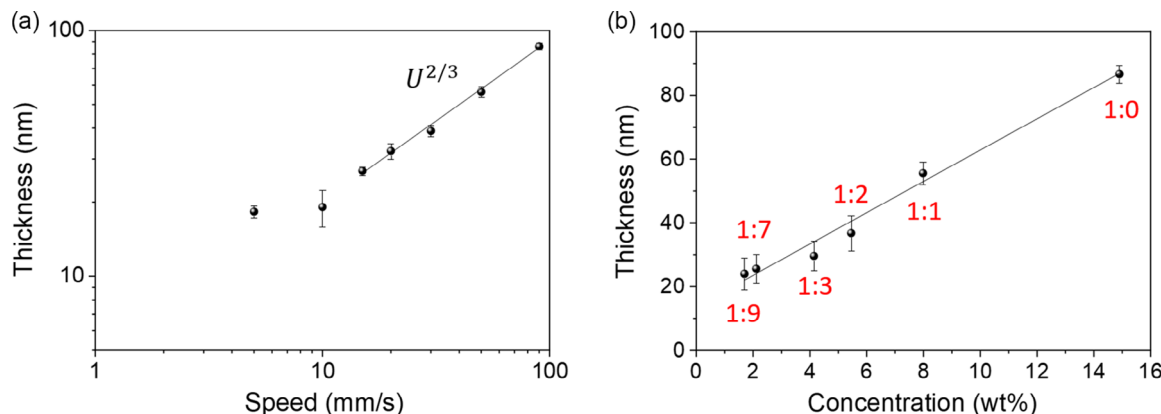


Figure 3. The influence on the dried film thickness by a) the coating speed and by b) the solution concentration (wt%) with indicated volume ratio $V_{\text{SnO}_2}:V_{\text{H}_2\text{O}}$ (in red).

evaporated solvent.^[22] However, higher blading speeds increase the viscous drag imposed on the meniscus, which yields a higher solution consumption and thus a thickness gradient along the coating direction as well as prolonged drying.

2.4. Impact of the Concentration

Besides the coating speed, we also study the influence of the solution concentration on the SnO₂ thickness. The concentration can be used to fine-tune the dried film thickness as it does not affect the drying process heavily, as e.g., the blading speed or the volume, since the wet film thickness is not increased. In Equation (1), the solution concentration is reflected in the numerical constant c_1 . We dilute the 14.9 wt% SnO₂ colloidal dispersion by deionized water with different volume ratios ranging from 1:0 to 1:9 and blade coat with 20 mm s⁻¹ on UVO-treated glass. As expected, the dried SnO₂ film thickness scales linearly with increasing concentration, as shown in Figure 3b. A linear trend is also maintained, when the coating speed changes to 15 or 30 mm s⁻¹ (Figure S10, Supporting Information). Having elaborated the influence of the blade coating parameters on film thickness and uniformity, we provide in Table S1, Supporting Information, an overview of each parameter and how it affects the dried film thickness.

2.5. Optimum SnO₂ Thickness by Blade Coating

To determine the optimum thickness of the blade-coated SnO₂ layer, we use different blading speeds, ranging from 10 to 90 mm s⁻¹, and concentrations, ranging from 1.69 wt% (volume ratio 1:9, V_{SnO₂}:V_{H₂O}) to 14.9 wt% (1:0, V_{SnO₂}:V_{H₂O}). The n-i-p device architecture is IOH/SnO₂/perovskite/Spiro-OMeTAD/Au and we measure the photovoltaic (PV) performance of over 36 cells per condition. Boxplots of the PV performance parameters are provided in Figure S11a, Supporting Information, for the blading speed and in Figure S11b, Supporting Information, for the concentration, while Figure S12a,b, Supporting Information, shows the PV performance depending on the film thickness obtained by different blading speeds and concentrations, respectively. Both series show a similar value of optimum SnO₂ layer thickness that yields the maximum power conversion efficiency (PCE), i.e., blading speed of 30 mm s⁻¹ or a concentration of 4.14 wt%, which corresponds to a film thickness of 30–35 nm. This thickness range also yields the highest open-circuit voltages (V_{OC}). The morphology and uniformity of these coating are checked by AFM (Figure S13a, Supporting Information) and SEM top-view images (Figure S13b, Supporting Information), which show smooth and compact SnO₂ films without pinholes, obtained with the optimized coating parameters. The heated substrate prevents the SnO₂ nanocrystals from aggregation in wet films. For thinner layers, the V_{OC} drops due to insufficient coverage on the IOH, as this causes serious charge carrier recombination. Beyond the optimum SnO₂ layer thickness, the V_{OC} again decreases due to less efficient charge extraction since more charges accumulate at the interface, which leads to an increased probability of charge carrier recombination.^[31,32] Regarding the short-circuit current density (J_{SC}), the trend is less clear, but generally, it decreases for higher coating speeds due to increased

parasitic absorption and internal reflections, as shown in the transmittance measurements for different film thickness controlled by the blading speed (Figure S14a, Supporting Information) and by the concentration (Figure S14b, Supporting Information). The fill factor (FF) value peaks for the same film thickness as for the V_{OC} are proving to be an optimum balance of sufficient substrate coverage and efficient charge transport.^[32–34] In Figure S15 and S16, Supporting Information, we further provide heat maps showing the spatial distribution of the PV performance values for varied coating speed and concentration of the solution, respectively. The heat maps further reveal localized thickness inhomogeneity due to operator-related factors as well as thickness gradients. For example, the location of the solution dispensing matters, since we cannot exclude that the dispensed solution will spread uniformly and create a homogeneous meniscus across the entire substrate width. In particular, the heat maps for 30 and 50 mm s⁻¹ show an overall performance drop where the solution is dispensed too far off the blade edge. Moreover, the heat maps of different concentrations show a trend of decreasing J_{SC} to the right hand side with respect to the blading direction. Multiple reasons can explain this observation, e.g., off-center dispensed solution, a blading gap deviation, inclined substrate placing, or a nonuniform sample illumination during the J–V measurement for these large substrate size.

2.6. Optimizing Spiro-OMeTAD Layer Deposition by Blade Coating

So far, the Spiro-OMeTAD hole transport layer (HTL) is deposited by spin coating for device fabrication. Now, we apply our understanding to blade coat Spiro-OMeTAD layer in ambient air with p-Xylene as solvent. This solvent has a slightly higher boiling point of 138 °C compared to the conventional solvent chlorobenzene (132 °C) which is normally used with Spiro-OMeTAD, but it is not halogenated, hence it is safer to use and more industrially compatible.^[35] Sufficiently thick Spiro-OMeTAD HTL film thickness is required to ensure a good coverage of the perovskite film. Therefore, we check the solubility of Spiro-OMeTAD in p-Xylene at room temperature to use the highest dissolvable concentration (25 mg mL⁻¹) of the solution and screen the blade coating speed of the Spiro-OMeTAD layer. The overview of the PV performance is presented in Figure S17, Supporting Information. The V_{OC} asymptotically approaches a constant value with small deviations when a coating speed of 30 mm s⁻¹ or higher is used, since the highest occupied molecular orbital (HOMO) energy level of Spiro-OMeTAD is independent of the thickness of the layer.^[36] Meanwhile, the J_{SC} and FF increase with higher coating speed enabled by proper surface coverage of the HTL on perovskite, leading to better charge extraction capability.^[37]

2.7. Champion Device

To improve the PV performance of the PSCs, we passivate the perovskite surface defects by spin coating the organic halide salt, phenethylammonium iodide (PEAI) on the perovskite absorber.^[13] The effectiveness of the PEAi passivation treatment

is shown in Figure S18, Supporting Information. PSCs were processed by combining the passivation treatment and optimized blade-coated SnO_2 and Spiro-OMeTAD layer. In Figure 4, we compare the PV performance of the sample with optimized blade-coated charge transport layers with the fully spin-coated sample. We achieve increased uniformity and V_{OC} with 44 devices on $50 \text{ mm} \times 50 \text{ mm}$ substrates when using blade-coated charge transport layers. The blade-coated champion device reaches a V_{OC} of 1.16 V for a 1.56 eV bandgap perovskite absorber and a PCE of 18.8% (Figure S19a, Supporting Information). Maximum power point (MPP) tracking yields a stabilized power output of 18.2 mW cm^{-2} (Figure S19b, Supporting Information). The external quantum efficiency (EQE) of the device shows an integrated J_{SC} that agrees well with the J_{SC} measured by the current–voltage scans (Figure S19c, Supporting Information). Reaching higher efficiencies is limited by low

FF due to improper oxidation of the Spiro-OMeTAD layer owing to lack of FK209 additive.^[38,39]

3. Conclusion and Outlook

In conclusion, our study sheds light on the various factors affecting the dried film thickness and uniformity of blade-coated SnO_2 nanoparticles. We systematically investigated the influence of the substrate temperature, dispensed solution volume, blade coating speed, and solution concentration on the dried film thickness of blade-coated SnO_2 nanoparticles. The substrate temperature improves the film uniformity along the coating direction by minimizing capillary flows. We show that film thickness and uniformity are affected by the advancing meniscus height. To demonstrate the influence of the dispensed solution volume and the

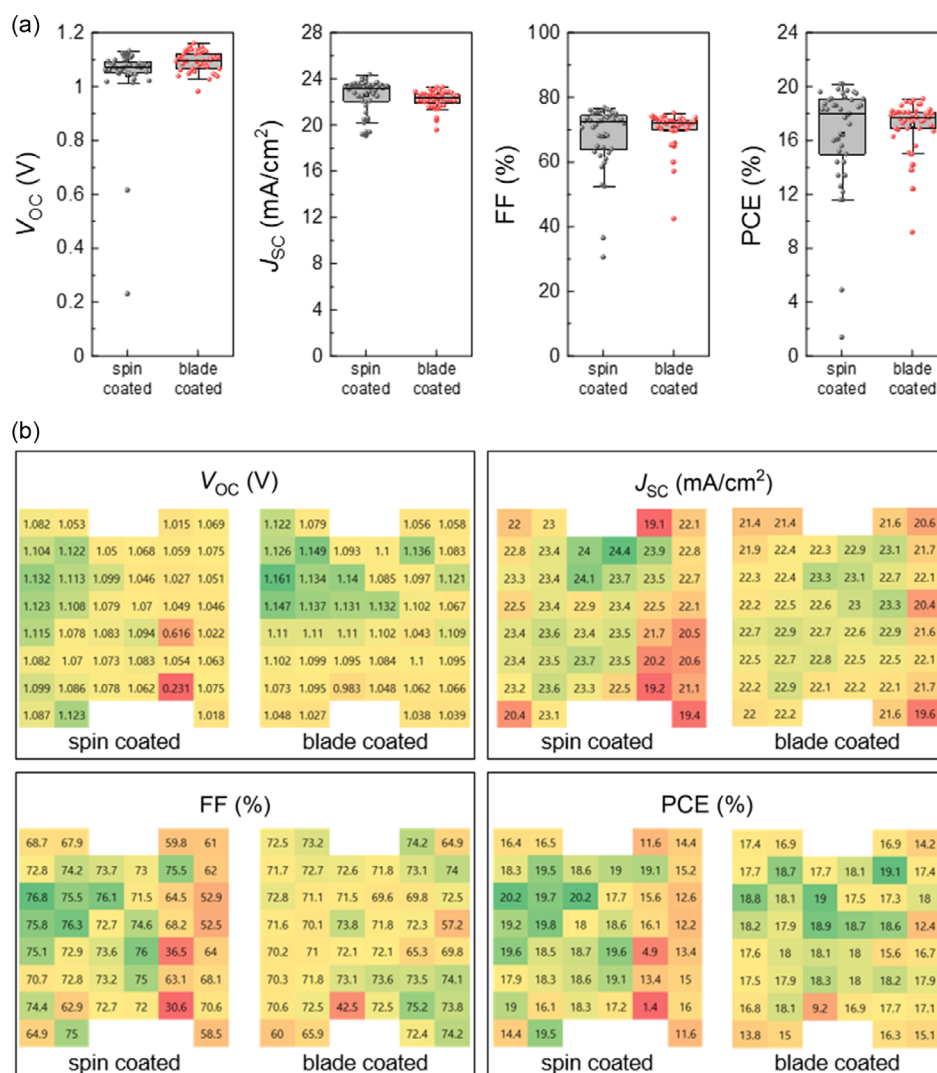


Figure 4. a) Comparison of PV performance parameters of over 36 devices of spin-coated (black) SnO_2 and blade-coated (red) SnO_2 while the Spiro-OMeTAD hole transport layer is also blade coated for both samples. b) Global heat maps of PV performance parameters of 44 devices to compare the uniformity of spin-coated SnO_2 and blade-coated SnO_2 while the Spiro-OMeTAD hole transport layer is also blade coated for both samples. A photograph of a $50 \text{ mm} \times 50 \text{ mm}$ sample layout is shown in Figure S20, Supporting Information.

blade angle on the film uniformity, we calculate the difference of the advancing meniscus height over the coating length, based on the solution consumption during the blade coating process. We present a modified setup with a solution reservoir to be adopted for large-area coatings with enhanced film uniformity. As a better option, we suggest equipping blade coating with a continuous solution supply, starting to broadly use slot-die coating for upscaling perovskite-based optoelectronic devices, and applying in situ characterizations to probe the thickness and uniformity of large coating areas.

Supporting Information

Supporting Information is available from the Wiley Online Library or from the author.

Acknowledgements

This work has received funding from the European Union's Horizon 2020 research and innovation program under grant agreement no. 850937 of the PERCISTAND project, the Swiss Federal Office of Energy (SFOE, Project HIPEROS, grant no. SI/502549-01), and the Swiss National Science Foundation (grant no. 200021_213073).

Open access funding provided by ETH-Bereich Forschungsanstalten.

Conflict of Interest

The authors declare no conflict of interest.

Data Availability Statement

The data that support the findings of this study are available from the corresponding author upon reasonable request.

Keywords

blade coating, perovskite solar cells, scalable deposition methods, SnO_2 electron transport layers

Received: April 13, 2023

Revised: May 16, 2023

Published online: May 25, 2023

- [1] H. Min, D. Y. Lee, J. Kim, G. Kim, K. S. Lee, J. Kim, M. J. Paik, Y. K. Kim, K. S. Kim, M. G. Kim, T. J. Shin, *Nature* **2021**, 598, 444.
- [2] S. De Wolf, J. Holovsky, S. J. Moon, P. Loper, B. Niesen, M. Ledinsky, F. J. Haug, J. H. Yum, C. Ballif, *J. Phys. Chem. Lett.* **2014**, 5, 1035.
- [3] M. M. Lee, J. Teuscher, T. Miyasaka, T. N. Murakami, H. J. Snaith, *Science* **2012**, 338, 643.
- [4] G. E. Eperon, S. D. Stranks, C. Menelaou, M. B. Johnston, L. M. Herz, H. J. Snaith, *Energy Environ. Sci.* **2014**, 7, 982.
- [5] W. J. Yin, T. Shi, Y. Yan, *Appl. Phys. Lett.* **2014**, 104, 063903.
- [6] M. Green, E. Dunlop, J. Hohl-Ebinger, M. Yoshita, N. Kipodakis, X. Hao, *Prog. Photovoltaics: Res. Appl.* **2022**, 30, 687.
- [7] Y. Deng, E. Peng, Y. Shao, Z. Xiao, Q. Dong, J. Huang, *Energy Environ. Sci.* **2015**, 8, 1544.
- [8] Z. Yang, C. C. Chueh, F. Zuo, J. H. Kim, P. W. Liang, A. K. Y. Jen, *Adv. Mater.* **2015**, 5, 1500328.
- [9] S. Castro-Hermosa, L. Wouk, I. S. Bicalho, L. de Queiroz Corrêa, B. de Jong, L. Cinà, T. M. Brown, D. Bagnis, *Nano Res.* **2020**, 14, 1034.
- [10] S. Siegrist, S. C. Yang, E. Gilshtein, X. Sun, A. N. Tiwari, F. Fu, *J. Mater. Chem. A* **2021**, 9, 26680.
- [11] Q. Wang, M. Eslamian, T. Zhao, A. K. Y. Jen, *IEEE J. Photovoltaics* **2018**, 8, 1662.
- [12] Q. Jiang, X. Zhang, J. You, *Small* **2018**, 14, 1801154.
- [13] Q. Jiang, Y. Zhao, X. Zhang, X. Yang, Y. Chen, Z. Chu, Q. Ye, X. Li, Z. Yin, J. You, *Nat. Photonics* **2019**, 13, 460.
- [14] J. J. Yoo, G. Seo, M. R. Chua, T. G. Park, Y. Lu, F. Rotermund, Y. K. Kim, C. S. Moon, N. J. Jeon, J. P. Correa-Baena, V. Bulović, *Nature* **2021**, 590, 587.
- [15] Z. Li, T. R. Klein, D. H. Kim, M. Yang, J. J. Berry, M. F. van Hest, K. Zhu, *Nat. Rev. Mater.* **2018**, 3, 18017.
- [16] B. Dou, J. B. Whitaker, K. Bruening, D. T. Moore, L. M. Wheeler, J. Ryter, N. J. Breslin, J. J. Berry, S. M. Garner, F. S. Barnes, S. E. Shaheen, *ACS Energy Lett.* **2018**, 3, 2558.
- [17] Y. Peng, F. Zeng, Y. Cheng, C. Wang, K. Huang, P. Xie, H. Xie, Y. Gao, J. Yang, *Org. Electron.* **2020**, 83, 105736.
- [18] T. Bu, J. Li, F. Zheng, W. Chen, X. Wen, Z. Ku, Y. Peng, J. Zhong, Y. B. Cheng, F. Huang, *Nat. Commun.* **2018**, 9, 4609.
- [19] M. Ernst, J. P. Herterich, C. Margenfeld, M. Kohlstädt, U. Würfel, *Sol. RRL* **2022**, 6, 2100535.
- [20] X. Niu, N. Li, Q. Chen, H. Zhou, *Adv. Energy Sustainability Res.* **2021**, 2, 2000046.
- [21] X. Dai, Y. Deng, C. H. Van Brackel, J. Huang, *Int. J. Extreme Manuf.* **2019**, 1, 022004.
- [22] M. Le Berre, Y. Chen, D. Baigl, *Langmuir* **2009**, 25, 2554.
- [23] L. Landau, B. Levich, *Dynamics of Curved Fronts* **1988**, pp. 141–153, <https://doi.org/10.1016/B978-0-08-092523-3.50016-2>.
- [24] X. Gu, L. Shaw, K. Gu, M. F. Toney, Z. Bao, *Nat. Commun.* **2018**, 9, 534.
- [25] J. Conway, H. Korn, M. R. Fisch, *Langmuir* **1997**, 13, 426.
- [26] R. D. Deegan, O. Bakajin, T. F. Dupont, *Nature* **1997**, 389, 827.
- [27] H. Hu, R. G. Larson, *J. Phys. Chem. B* **2006**, 110, 7090.
- [28] R. L. Davis, S. Jayaraman, P. M. Chaikin, R. A. Register, *Langmuir* **2014**, 30, 5637.
- [29] Y. Deng, X. Zheng, Y. Bai, Q. Wang, J. Zhao, J. Huang, *Nat. Energy* **2018**, 3, 560.
- [30] M. K. Kim, H. S. Lee, S. R. Pae, D. J. Kim, J. Y. Lee, I. Gereige, S. Park, B. Shin, *J. Mater. Chem. A* **2018**, 6, 24911.
- [31] R. Jeyakumar, A. Bag, R. Nekovei, R. Radhakrishnan, *J. Electron. Mater.* **2020**, 49, 3533.
- [32] S. A. Moiz, *Photonics* **2021**, 9, 23.
- [33] D. Bartsaghi, I. D. C. Pérez, J. Kniepert, S. Roland, M. Turbiez, D. Neher, L. J. A. Koster, *Nat. Commun.* **2015**, 6, 2.
- [34] A. A. Eliwi, M. M. Byranvand, P. Fassl, M. R. Khan, I. M. Hossain, M. Frericks, S. Ternes, T. Abzieher, J. A. Schwenzer, T. Mayer, J. P. Hofmann, *Mater. Adv.* **2022**, 3, 456.
- [35] F. Isabelli, F. Di Giacomo, H. Gorter, F. Brunetti, P. Groen, R. Andriessen, Y. Galagan, *ACS Appl. Energy Mater.* **2018**, 1, 6056.
- [36] G. W. Kim, D. V. Shinde, T. Park, *RSC Adv.* **2015**, 5, 99356.
- [37] A. Bag, R. Radhakrishnan, R. Nekovei, R. Jeyakumar, *Sol. Energy* **2020**, 196, 177.
- [38] A. Abate, T. Leijtens, Patha, S. k, J. Teuscher, R. Avolio, M. E. Errico, J. Kirkpatrick, J. M. Ball, P. Docampo, I. McPherson, H. J. Snaith, *Phys. Chem. Chem. Phys.* **2013**, 15, 2572.
- [39] T. M. Koh, S. Dharani, H. Li, R. R. Prabhakar, N. Mathews, A. C. Grimsdale, S. G. Mhaisalkar, *ChemSusChem* **2014**, 7, 1909.